

1 **Seismic velocity structure of seaward-dipping reflectors on** 2 **the South American continental margin**

3 Carl McDermott¹, Jenny S. Collier^{1*}, Lidia Lonergan¹, Juergen Fruehn², Paul Bellingham²

4 * Corresponding author

5 ¹*Dept. Earth Science & Engineering, Imperial College London, Exhibition Road, London, SW7*
6 *2AZ, UK.*

7 ²*ION-GXT, 31 Windsor Street, Chertsey, Surrey, KT16 8AT, UK.*

8 **1 Abstract**

9 Seaward dipping reflectors (SDRs) are a key feature within the continent to ocean transition
10 zone of volcanic passive margins. Here we conduct an automated pre-stack depth-migration
11 imaging analysis of commercial seismic data from the volcanic margins of South America.
12 The method used an isotropic, ray-based approach of iterative velocity model building
13 based on the travel time inversion of residual pre-stack depth migration move-out. We find
14 two distinct seismic velocity patterns within the SDRs. While both types show a general
15 increase in velocity with depth consistent with expected compaction and
16 alteration/metamorphic trends, those SDRs that lie within faulted half grabens also have
17 high velocity zones at their down-dip ends. The velocity anomalies are generally concordant
18 with the reflectivity and so we attribute them to the presence of dolerite sills that were
19 injected into the lava pile. The sills therefore result from late-stage melt delivery along the
20 large landward-dipping faults that bound them. In contrast the more outboard SDRs show
21 no velocity anomalies, are more uniform spatially and have unfaulted basal contacts. Our
22 observations imply that the SDRs document a major change in rift architecture, with

23 magmatism linked with early extension and faulting of the upper brittle crust transitioning
24 into more organised, dike-fed eruptions similar to seafloor spreading.

25 **Keywords:**

26 Continental breakup; Volcanic passive margins; Seaward-dipping reflectors; tomographic
27 inversion

28 **2 Introduction**

29 Seaward-dipping reflectors (SDRs), with their characteristic wedges of oceanward-diverging
30 reflectors, were first recognised on seismic profiles in the 1980s (Hinz, 1981; Mutter et al.,
31 1982). They have since been shown to be a common feature within the continent to ocean
32 transition zone of volcanic passive margins worldwide (e.g. Franke, 2013). Drilling showed
33 them to consist of sub-aerially erupted basaltic lava flows interbedded with thinner layers of
34 volcanic tuff and terrestrial sediment (Roberts et al., 1984; Eldholm et al., 1987; Larsen et
35 al., 1994). Several studies have shown how this layering causes seismic scattering, complex
36 multiples and mode conversions (Planke et al., 1999; Ziolkowski et al., 2003). On mature
37 margins the SDRs are generally buried beneath kilometres of post-rift sediments which
38 often results in interference from the sea-bed multiple and further limited their early
39 interpretation. These issues combined to restrict early attempts to image their lowermost
40 parts and their important contacts with the basement. The geological process responsible
41 for the characteristic SDR geometry and the nature of the underlying rift architecture is
42 therefore an outstanding question.

43 Due to the seismic imaging issues summarised above and the restriction of most boreholes
44 to the upper parts of the most landward sequences, much of our current understanding of

45 SDRs draws on observations from rare onshore exposures and modern-day analogues. For
46 example, exhumed flanks along southeast Baffin, west Greenland and east Greenland
47 display arrays of landward-dipping normal faults with kilometre-scale offsets that are
48 intimately associated with syn-rift volcanism (Geoffroy et al., 2001; Geoffroy, 2005). Along
49 southeast Greenland, where the depth of erosion is deepest, gabbroic bodies which are
50 interpreted to represent the solidified and depleted magmatic source of the overlying lavas
51 are found within the continental basement (Myers, 1980; Brooks and Nielsen, 1982; Klausen
52 and Larsen, 2002). These observations suggest that syn-rift volcanism and footwall rotation
53 could be responsible for SDR formation in the early break-up stages at least. This idea has
54 been supported by the limited offshore drilling in the North Atlantic (Gibson and Love, 1989;
55 Larsen et al., 1994). However, critics of this model for the origin of SDR geometries cite the
56 lack of evidence for large landward dipping faults within active rift areas such as Ethiopia
57 (Corti et al., 2015).

58 The earliest published SDR formation models used comparisons with the Tertiary lava
59 sequence in eastern Iceland to emphasise the role of volcanic loading onto a weak
60 lithosphere in the generation of accommodation space and reflector dips (Hinz, 1981;
61 Mutter et al., 1982). This flexural mode of SDR formation by steady-state, sub-aerial seafloor
62 spreading has more recently been developed by Buck (2017) and Morgan and Watts (2018).
63 In these models the flexural load consists of solidified feeder dykes added to the edge of a
64 thin elastic plate. Distinct SDR wedges are formed by jumps in the location of dyke injection
65 or hiatuses during the continental extension process. In the current scientific literature
66 these two mechanisms (footwall rotation and magmatic loading) have been regarded as

67 competing. Establishing the correct mechanism clearly has important implications for the
68 rheology of the continental lithosphere during the transition to seafloor spreading.

69 A recent impetus from deep-water hydrocarbon exploration has resulted in the next
70 generation of 2D seismic imagery being collected which is pushing forward our knowledge
71 of the process of continental breakup at volcanic margins (e.g. Quirk et al., 2014; Stica et al.,
72 2014; Abdelmalak et al., 2015). By using long hydrophone streamers and deep-towed
73 sources rich in low frequencies it is now possible to resolve the internal structure and even
74 penetrate thick SDR sequences. For the first time conclusive evidence for fault-bounded
75 SDRs has been documented offshore, with several authors proposing hybrid models
76 containing a combination of faulting and flexure as controls on SDR geometry (Quirk et al.,
77 2014; Paton et al., 2017).

78 A promising aspect of the new generation data is the ability to extract robust seismic
79 velocities from the extrusive volcanic sequences to aid their interpretation (e.g. Ogilvie et
80 al., 2001; Spitzer et al., 2005; Goncharov and Nelson, 2012). An advantage of this method is
81 that it produces results that are typically an order of magnitude finer than conventional
82 wide angle imaging using seabed receivers and surface shots (e.g. White et al., 2008).
83 Within the continent-ocean transition zone seismic velocity is a particularly sensitive
84 parameter to rock lithology (igneous and sedimentary) together with porosity, pore aspect
85 ratio and alteration.

86 The aim of this study is to apply an automated pre-stack travel-time tomographic inversion
87 to two long-offset, surface-towed seismic reflection profiles from the volcanic margins of
88 South America. To our knowledge an analysis of this type has not previously targeted SDR
89 sequences across an entire volcanic continental margin. By determining the velocity

90 structure we will gain insights into the origins of SDRs and hence place new constraints on
91 the process of continental breakup.

92 **3 Previous work**

93 We previously presented an interpretation of a set of industry-standard, 2D seismic
94 reflection profiles and magnetic anomaly data from the volcanic margins of the South
95 Atlantic (McDermott et al., 2018; Collier et al., 2017). The seismic dataset was acquired by
96 *ION Geophysical* between 2009 and 2012 with a 10.2 km long-offset 408-channel streamer,
97 a 50 m shot interval and a tuned air gun array with a volume of 6420 in³. The complete
98 seismic survey comprises 25 dip- and 15 strike- pre-stack, depth-migrated (PSDM) sections,
99 with a total line length of almost 22,000 km that covers offshore Argentina, Uruguay and
100 southern Brazil (the Pelotas Basin). The Paraná continental flood basalt province lies
101 onshore the northern part of the study area (Figure 1).

102 The SDRs extend near continuously from southern Argentina to the Pelotas Basin (Figure 1).
103 They have an across margin width of 70-120 km in the south which increases dramatically to
104 > 300 km in the north. Several boreholes have penetrated the most-landward parts of these
105 sequences and have confirmed the presence of basaltic flows with weathered tops,
106 interbedded with terrestrial sediments (Gordon and Mohriak, 2015). Individual flows are
107 typically between 0.5 and 18 m thick, which is less than the 20-40 m vertical resolution of
108 the seismic reflection data. This implies the reflectors themselves do not represent
109 boundaries between individual “hard” lava flows and “soft” interbedded sediments but
110 from groups of these layers constructively interfering (Planke and Eldholm, 1994).

111 In our recent study we chose not to apply the “inner” and “outer” SDR terms established by
112 Planke et al. (2000). Instead, we introduced new terminology to describe the characteristics
113 of the SDRs: Type I and Type II. An important distinction is that offshore South America
114 there are not two spatially distinct sets of SDRs, but rather they onlap each other. This
115 distinction has been previously noted by Franke et al. (2010) and Soto et al. (2011). Due to
116 the association of the SDRs with other volcanic features such as lava deltas, we interpret
117 them all as subaerial. A summary of the key characteristics of the two SDR types is given in
118 Figure 2. The seismic imagery is now of sufficient quality to interpret the presence of
119 rotated fault blocks beneath the landward flows. We termed these SDRs as Type I to
120 distinguish them from the more seaward Type II SDRs that are unfaulted and either stack on
121 top of the Type Is or have a relatively flat contact with the underlying basement. Type I are
122 both shorter and straighter reflection packages that form fault-bounded wedges. The Type II
123 reflectors form concave downward, off-lapping reflection packages, with dips increasing at
124 their distal ends (McDermott et al., 2018).

125 In terms of distribution, the Type I SDRs have uniform widths and thicknesses along the
126 entire margin studied, whereas the Type II SDRs become significantly wider and thicker in
127 the north, co-incident with the onshore Paraná flood basalt province (Figure 1). In this
128 region, individual reflectors also become significantly longer and so we subdivide the Type II
129 SDRs into IIa in the south and IIb in the north. The most likely explanation for the longer
130 flow lengths in the north is higher topographic elevation due to anomalously hot
131 asthenosphere at the time of breakup. This is consistent with the rapid increase in the
132 volume of SDRs and also an increase in the thickness of the oceanic crust in this area
133 (Taposeea et al., 2016). Independent interpretations of subsets of the commercial seismic

134 data used by us have been presented in the Pelotas (Stica et al., 2014) and Uruguay regions
135 (Paton et al., 2017; Conti et al., 2017). These authors also document the presence of both
136 faulted and non-faulted SDRs.

137 For our seismic velocity inversion analysis we selected two multichannel seismic reflection
138 profiles that represent the key characteristics of the SDRs along the margin (Figure 3). For
139 both lines the post-rift does not present any specific imaging challenges, such as salt, free
140 gas, channels etc., so we could focus on model building within the SDRs. The quality of the
141 depth imaging on both lines is demonstrated by the presence of significant reflectivity
142 below the SDRs, either in the form of lower-crustal reflectivity and/or what is interpreted as
143 Moho. This allows a confident interpretation of the base of the SDRs where the reflectivity
144 abruptly terminates. Line A is from offshore Uruguay and displays three packages of classic
145 Type I SDRs, the most oceanward of which is partially overlain by a volumetrically modest
146 Type IIa sequence with characteristically short reflectors. The SDRs reach a maximum
147 thickness of around 4 km, which is in marked contrast to Line B, which lies immediately
148 offshore the Paraná of southern Brazil, where they exceed 12 km. Two packages of Type I
149 SDRs are also visible on Line B (x=35-80 km, Figure 3), but they are both overlain by thick
150 Type IIb SDR units with characteristically long reflectors. This profile crosses a tectonic
151 transfer zone that developed into the Chui Fracture Zone once seafloor spreading got
152 underway (Figure 1). This zone is clearly seen in the seismic by uplifted basement blocks and
153 results in a set of landward dipping SDRs (x=185-210 km).

154 **4 Method**

155 The seismic velocity models were generated with a PSDM tomographic method (Jones,
156 2010). This solves for the travel times between the source and receivers by finding the

157 isotropic velocity model that best flattens primary reflection events across offsets within
158 common reflection point (CRP) gathers. The starting velocity model for each profile
159 consisted of a combination of a mature tomographic inversion model for the post-rift
160 sediments with one developed from manual semblance picks across the SDRs every 750 –
161 1000 m. The manual part of the model was smoothed laterally and vertically to remove any
162 local artefacts and the maximum velocity was capped at 6 km/s. This removed any potential
163 biases towards high velocities along the base of the SDRs.

164 The raw time gathers were pre-stack depth migrated with a Kirchhoff algorithm in shortest
165 ray-path mode. Tests showed that a migration aperture of 6000 m and a maximum dip limit
166 of 65° ensured that most of the primary SDR signal was included. The CRP gathers were then
167 conditioned to reduce multiples and high-frequency noise within the SDRs. A Tau-P Radon
168 multiple suppression scheme was used with a P-range of 3000/-100 ms and a P-cut value of
169 150 ms at 10.2 km offset (Figure 4a-c). This was followed by a 3-6-30-40 Hz Ormsby
170 bandpass filter. Finally, an angle-mute of 45⁰, combined with an x-z mute to reduce NMO-
171 stretch at deeper levels was applied (Figure 4d-e). The coherency (or semblance) was then
172 calculated at each depth point across all offsets, with a value of 1 indicating perfect
173 horizontal alignment.

174 The residual move-out for each horizon across all offsets was then calculated using a
175 wavelet tracking technique (Jones, 2010). Horizon seed points were made on the zero-offset
176 trace on every fifth CRP (75 m) if its amplitude exceeded a given threshold and the
177 coherency exceeded 0.5. In general, the vertical spacing between seed points within the
178 SDRs was on the order of 50 - 100 m. The residual move-out picks were only used if the
179 autotracker could follow an event for least 70% of the total (muted) offset.

180 The selected move-out residuals were then input into a tomographic inversion scheme that
181 uses a conjugate-gradient (damped least squares) solver to update the velocity field (Fruehn
182 et al., 2014). The method incorporated “hard constraint layers”, above which the velocity
183 was fixed during the inversion. This allowed a “layer stripping” approach to be applied, with
184 successively deeper levels within the post-rift sediment overburden being fixed as the
185 inversion progressed. A 500 m (20 CRP) horizontal by 200 m depth cell size was found to
186 give the most stable inversion results for the target (SDR) region. The velocity solver
187 accounts for both the dip and depth of a reflection by scanning through an appropriate
188 stacked image (made with either the previous tomographic model or a model update
189 derived from 2nd order residual move-out picks) within a user defined window. The
190 algorithm assumes that structures within this window can be approximated by a plane. If
191 the assumption is broken, it will result in incorrect dips and poor signal coherency which
192 will, in turn, reduce the residual pick density within each inversion cell. It is therefore better
193 to use a smaller window in areas of high dip. A relatively small window size (7 CRPs x 35 m)
194 was used to account for the higher dips present towards the base of the SDR sequence.
195 Events with dips greater than 40° were ignored during updates.

196 After each iteration the quality of the output model was visually checked for the presence of
197 anomalous velocity contrasts such as localised horizontal or vertical striping. Most
198 irregularities were small and could be corrected for by smoothing the model or by
199 increasing the cell size during inversion. The change in the flatness of the CRP gathers was
200 also visually reviewed (Figure 5). A better model produced flatter gathers to longer offsets
201 whilst maintaining geologically reasonable velocities. If the quality of the CRP gathers
202 deteriorated, the residual depth picks would be assessed and the inversion re-run. Once a

203 velocity model update was deemed acceptable it was used as input for the next
204 tomographic run. In practice, the process of residual move-out tracking, tomography and
205 remigration was stopped after three iterations as this was judged to result in optimal
206 flatness of the gathers across the profiles. In order to highlight where the seismic velocity
207 field was well-constrained by the data the final coherence values were averaged onto a
208 10x0.6 km grid and a bulk coherency threshold of 0.3 used in our interpretation.

209 **5 Results**

210 The final interval velocity models are presented as underlays to the pre-stack depth-
211 migrated seismic sections to show their relationship with the reflectivity in Figures 6 and 7.
212 Enlarged versions, together with interpretations, are given in Figures 8 and 9. In these
213 figures the bulk coherence threshold is marked with the white dashed line. Velocities below
214 this line are not constrained by the tomographic inversion and should be ignored. As can be
215 seen the entire SDR sequence for Line A is above the coherence threshold, and most of the
216 SDR sequence for Line B. To compare velocity-depth trends we extracted vertical profiles
217 across the SDRs at 1 km along-profile intervals and present them individually (Profiles i-iv,
218 Figures 8d, 9d) or stacked (Figures 8e, 9e).

219 The post-rift sedimentary sequence displays velocities increasing from 1.8 to 4.5 km/s with
220 depth, consistent with expected compaction trends for terrigenous sediment (Hamilton,
221 1979). Overall, the velocity gradient is similar throughout but because sediment thickness
222 ranges between 3 and 6.5 km the velocity contrast at the top of the SDRs varies. In places
223 there is a small positive velocity step as the SDRs are entered (e.g. Profiles i and ii, Figure 8),
224 but elsewhere there is a smoother transition and the picking of the Top SDR horizon relied
225 on a change of reflectivity character. The seismic velocity within the uppermost SDRs ranges

226 between 3.0 and 4.8 km/s, with higher velocities where the SDRs are more deeply buried
227 (Figures 8e, 9e). The maximum seismic velocity recorded in the SDRs is 7 km/s.

228 Within the upper 1-2 km of SDRs, there is a steep velocity gradient (0.5-1 /s) everywhere.
229 When the velocity reaches ~5.5 km/s the gradient reduces to 0.25-0.5 /s. However, whilst
230 the upper parts of the SDRs show similar velocity-depth characteristics, the lower parts do
231 not. Instead we observe two contrasting velocity patterns which directly correlate with the
232 two SDR types we identified previously. The Type I SDRs on Line A are laterally variable with
233 three distinct velocity highs at their down-dip ends (Figures 6 and 8). Individual velocity
234 highs are typically 4-6 km wide, 2-3 km thick and spaced 10 km apart, with velocities
235 reaching 6.5-6.8 km/s. We are confident about the presence of these high velocity features
236 as they were also identified during the manual semblance analysis. They were deliberately
237 removed from the starting model by capping at 6 km/s but were consistently reintroduced
238 by the tomographic inversion. The locations of these high velocity zones correlate with the
239 basement-bounding faults interpreted from the reflectivity alone. Note that this pattern is
240 not seen within the Type I SDRs imaged on Line B (Figures 7 and 9), but this is entirely
241 consistent with their much deeper burial and subsequent rotation by the huge volumes of
242 the later Type IIb SDRs, which may have resulted in the velocity contrasts at the down-dip
243 portions being undetected.

244 In contrast to the Type I SDR pattern both the Type II SDRs continue to show a moderate
245 positive velocity gradient with depth (Figures 8d and 9d), with sub-horizontal velocity
246 contours that crosscut the dipping reflectors (Figures 8b and 9b). Distinct velocity highs are
247 absent. This uniformity of the Type II velocity-depth profiles can be readily seen from the

248 narrow range within the stacked profiles of Figures 8e and 9e, which are in marked contrast
249 to the broad spectrum of velocities obtained across the Type I SDRs.

250 The velocity inversion has also provided new constraints on the nature of the top ~5 km of
251 the basement below the SDRs for the first 50 km or so of the continental (western) ends of
252 both profiles. Overall the continental velocities are about 0.5 km/s higher on Line B than
253 Line A. This may be a result of the thicker sedimentary sequence closing micro-fractures and
254 pores within the basement or higher volumes of igneous intrusion within the continental
255 crust. The latter interpretation is supported on Line A by the presence of two high-velocity
256 regions where interval velocities reach 6.8 km/s ($x=25-50$ km, $z=5-12$ km). Similarly, on Line
257 A a ~50 km portion of oceanic crust ($x=145-170$ km), with seismic velocities reaching 7.2
258 km/s within the semblance threshold on the eastern end of the line. Line B terminates
259 before full oceanic crust is developed.

260 **6 Discussion**

261 **6.1 Result validation**

262 In our study we have used software routinely applied by us for the commercial imaging of
263 hydrocarbon targets. In many cases, the validity of the method has therefore been
264 independently confirmed (e.g. Fruehn et al., 2014). Many of the previously published
265 studies that extract velocities from surface-towed hydrophone data have focussed on the
266 so-called “sub-basalt imaging” problem on the NW European shelf (notably in the Faeroe-
267 Shetland area). Here thick, flat-lying basaltic layers overlie potential hydrocarbon reservoir
268 rocks (e.g. Fliedner and White, 2001). Various approaches to velocity extraction have been
269 used and in some cases the results could be directly compared to downhole sonic logs that
270 had been calibrated with VSP/check-shot surveys. These comparisons are typically within

271 0.1 km/s (3-5%,) and we expect our accuracies to be similar (Ogilvie et al., 2001, Fruehn et
272 al., 2008).

273 For our study, Independent validation of the seismic velocity results across the SDRs comes
274 from wireline logs in the region of Line B (Gordon and Mohriak, 2015) and BGR04-REFR01
275 wide-angle seismic profile that is co-incident with Line A (Becker et al., 2014). In the
276 boreholes (see Figure 1 for locations) the wireline logs show lava flow interior velocities
277 range between 4.6-6.2 km/s, with flow tops and interbedded sediments falling to 3.0 km/s.
278 Given the vertical resolution in our new models is 200m and individual lava flows are 0.5-18
279 m thick, the velocities extracted from the seismic data will depend on the relative
280 proportions of flows and sediment interbeds together with the thickness of the flows. The
281 seismic velocities we have obtained at the landward-top of our SDR sequences on Line B
282 (e.g. profile iv 4.7 km/s, Figure 9d) are therefore entirely consistent with the available
283 wireline-logs.

284 In the BGR04-REFR01 wide-angle seismic model velocities range between 4.5 km/s at the
285 top to 6.5 km/s at the base of the SDRs (Becker et al., 2014). These values compare
286 favourably with our Line A, where they range between 3.5 and 6.8 km/s. To compare the
287 results in more detail we show a velocity-depth profile extracted from the wide-angle model
288 at the location of our profile ii (black line, Figure 8d). As can be seen there is an overall good
289 match between the results, both in the sediments and SDRs, with the two profiles differing
290 less than 0.5 km/s. Receiver spacing for the wide-angle experiment was 20 km, and so its
291 velocity model did not detect any lateral velocity variation across the SDRs and specifically
292 any velocity highs. We note however that our seismic model shows slightly faster SDR
293 velocities throughout than the wide-angle model. Possibly this is a result of anisotropy i.e.

294 the variation of seismic velocity with direction of travel between our (near vertical) and
295 wide-angle (near horizontal) acquisition. SDR sequences have been shown to exhibit
296 transverse anisotropy on the order of 10-15% (Planke et al., 1999). This possibility however
297 would need to be confirmed by comparison with a higher quality wide-angle profile with
298 closer instrument spacing.

299 **6.2 Composition, compaction and alteration trends**

300 In order to compare the velocities of the SDR sequences across the margins and to try to
301 separate the effects of composition changes from compaction and alteration trends in the
302 data we followed the approach taken by Goncharov and Nelson (2012) and converted the
303 extracted profiles from depth to lithospheric pressure. We use a simple 3-layer model
304 (water, sediment and SDR with densities of 1000, 2200 and 2800 kg/m³ respectively) to
305 correct for the variation in the overburden thicknesses (Figure 10). This approach shows
306 that although the velocities are lowest at the top of the Type IIb SDRs, this unit has the
307 lowest overburden pressure. When compared at equivalent pressures, the Type IIa SDRs
308 actually display the lowest velocities i.e. at the top of Type IIa (150 MPa) velocities are
309 between 4.3-5 km/s compared to 5.5-6.3 km/s for Type IIb at the same pressure. The
310 simplest explanation for this difference is an increase in the relative volcanic component
311 and/or an increase in average flow thickness towards the Paraná volcanic province. The
312 velocities of the Type I SDRs are the most variable, suggesting that there is much greater
313 heterogeneity within these SDRs. This is consistent with their landward location and
314 association with large normal faults in a sub-aerial rift environment that would be expected
315 to deliver higher levels of spatially variable terrigenous sediment compared to the Type II

316 SDRs which according to our interpretation are equivalent to subaerial seafloor spreading in
317 the later stage of breakup.

318 In order to further investigate the seismic-velocity depth trends we made a comparison with
319 seismic velocity profiles obtained from a field experiment in Iceland (Darbyshire et al.,
320 1998). Here, because of the mid-ocean setting continental sediments can be assumed to be
321 minimal and so the trends can be interpreted as a response of extruded basalt to
322 compaction and alteration. On Iceland, the overall pattern of the velocity-depth trend is
323 very similar to that seen in our Type IIb SDRs. This further supports the idea that the
324 difference between the seismic velocity of the Type IIa and IIb SDRs results from an increase
325 in lava content northwards along the margin. The very different Type I SDR trend reinforces
326 the idea that these early SDRs were formed by a different mechanism than the subaerial
327 seafloor-spreading that generated both the Type II SDRs and the upper Icelandic crust.

328 The Type II SDRs document a change in velocity gradient at about 200 MPa. The Icelandic
329 profiles have a similar pattern, but with an inflection point slightly shallower (160-180 MPa).
330 The frequency bandwidth of the seismic reflection data we used is 5-50 Hz (at the 20 dB
331 level) within the SDR sequence, giving a limiting vertical resolution of 25 m. Within this level
332 of resolution the reflectivity images give no indication of any change in the nature of the
333 basaltic flows and interbeds, so we interpret the velocity-depth patterns in terms of
334 compaction and alteration trends. In oceanic crust there is a similar seismic velocity gradient
335 change at the Layer 2/3 boundary which has also been interpreted as an alteration front
336 within the sheeted dykes (Detrick et al., 1994). We interpret the rapid velocity gradients at
337 the top of the Type II SDRs as due to compaction (i.e. reduction in porosity) of the volcanic-
338 sedimentary sequence in response to increasing burial depth. Borehole observations have

339 shown that mechanical compaction within lava flows is generally minimal, so much of the
340 change is likely to be due to the sedimentary interbeds (Planke and Eldholm, 1994). In the
341 mid-to-lower part of the Type II SDRs, the smaller gradients are likely to be due to
342 metamorphism under zeolite to granulite facies. The maximum velocity (~ 7 km/s) within the
343 deepest Type IIb SDRs is consistent with the values measured by Christensen (1996) for
344 greenschist facies basalt at 400 MPa (6.88 ± 0.2 km/s). It seems likely therefore that the
345 velocity structure observed in the Type II SDRs results from (i) diagenetic compaction of the
346 volcanic/sedimentary sequence (upper SDRs) followed by (ii) gradual alteration of the
347 basalts to low-grade zeolite facies basalts (middle SDRs) and greenschist facies basalts
348 (lower SDRs). Similar conclusions were made by Mjelde et al. (2007) from wide-angle
349 seismic models of the Norwegian margin.

350 **6.3 Type I high velocity bodies**

351 To our knowledge velocity highs have not been previously detected at the seaward end of
352 any SDR packages worldwide. Given the velocity highs exceed the compaction and alteration
353 related velocity trends established by the Type II SDRs, the most plausible explanation for
354 them is either a lateral change in the ratio of volcanic to sedimentary rock, the presence of a
355 different volcanic rock type and/or mode of emplacement (i.e. not extrusive). Velocity in
356 these regions reach 6.5 - 6.8 km/s which is consistent with the measured velocity of dolerite
357 (6.71 ± 0.27 km/s) at similar pressures (Christensen, 1996). We favour an interpretation of
358 the presence of a different rock type because of the geometrical relationship with the SDR
359 packages. The velocity highs are associated with continuous reflectors and so our preferred
360 interpretation is that they are late-stage sills injected deep within the lava flow pile. Similar
361 bodies have been imaged within sedimentary sequences in the Voring Basin of Norway

362 (Berndt et al., 2000). Here up to 100 m thick olivine-gabbroic sills have been sampled and
363 shown to give local seismic velocity anomalies of up to 7.4 km/s. They tend to occur in
364 groups, within a vertical interval of 2-3 km and individual sill lengths of up to 5 km. These
365 dimensions are similar to the high velocity zones seen in our images (Figure 8). In our case,
366 late-stage injection into the lava pile would provide the conditions for slow cooling and so
367 growth of large crystals that increases the seismic velocity relative to the surrounding
368 extrusive basalts. The magma would have been sourced from a plumbing system that
369 exploited the higher permeability along the fault systems that now bound the Type I SDR
370 packages and explains their restriction to the down-dip portion of the SDRs. This
371 interpretation is consistent with our analysis of the magnetic properties of this region,
372 where Type II SDRs were found to correlate with linear magnetic anomalies but Type I SDRs
373 did not (Collier et al., 2017). The eruption of Type II SDRs marks a period of more-organised
374 volcanism, where linear fissures can be maintained to feed significant volumes of magma.
375 The two SDR types undoubtedly mark a transition from fault-dominated extension in the
376 continental crust to magmatic-dominated extension in the oceanic domain.

377 **7 Conclusions**

378 We have generated velocity models across a set of SDRs from two commercial seismic
379 reflection profiles in the South Atlantic using commercial in-house software and expertise.
380 Our analysis has provided constraints on the physical properties of the material to
381 supplement the reflector geometries provided by the stacked sections. The method used an
382 isotropic, ray-based approach of iterative velocity model building based on the travel time
383 inversion of residual pre-stack depth migration move-out. This is far superior to
384 conventional semblance analysis in the time-domain, and provides velocity estimates of

385 high fidelity. Velocity models with a vertical and lateral resolution of 200 and 500 m
386 respectively were generated together with formal uncertainty bounds. Our work shows:

- 387 • The two classes of SDR identified from their reflectivity and magnetic properties
388 (McDermott et al., 2018; Collier et al., 2017) correlate with distinct seismic velocity
389 patterns. The velocities of the Type I SDRs are the most variable, suggesting that
390 there is much greater heterogeneity within these SDRs.
- 391 • The Type II (non-fault bounded) SDRs display seismic-velocity depth trends
392 consistent with compaction and alteration. We interpret the trend as due to (i) the
393 diagenetic compaction of the volcanic sequence (upper SDRs) followed by (ii) the
394 gradual alteration of the compacted basalts to low-grade zeolite (middle SDRs) and
395 then greenschist facies basalts (lower SDRs). Those closer to the onshore Paraná
396 flood basalt province (Type IIb) have higher pressure-corrected seismic velocities
397 suggesting they contain a higher proportion of extrusive volcanic rock. Our
398 interpretation of the Type II SDRs bears a strong similarity to the Tertiary lava flow
399 sequence exposed in Iceland.
- 400 • The Type I (fault bounded) SDRs show seismic velocity highs at their down dip ends
401 which we interpret as doleritic sills that were injected into the lava pile. This magma
402 was supplied from feeder systems that exploited the large landward dipping faults
403 that bound the packages and control their geometries.

404 Our work implies that both the tectonic footwall rotation and flexural-magmatic loading
405 model for SDR generation operate, but at different stages of breakup. The fault-
406 controlled (Type I) SDRs are less voluminous and may be deeply buried by the magmatic-

407 loading controlled (Type II), which explains why they have been missed in many previous
408 studies of volcanic continental margins.

409

410 **8 Figure captions**

411 **Figure 1.** Topographic map of the study area showing seismic line coverage, margin
412 segmentation and spatial extents of the two types of SDR (McDermott et al., 2018). The
413 locations of the two seismic profiles presented here are marked with the bold lines.

414 **Figure 2.** A summary of features of SDR types identified from our previous interpretation of
415 reflectivity and magnetic anomaly data. Note the different length scales of the sketches. See
416 McDermott et al., 2018 and Collier et al., 2017 for further details.

417 **Figure 3.** PSDM images of the two seismic reflection profiles used in this study. Note that
418 the sections are plotted with the same vertical exaggeration to allow a comparison of dips.
419 The lateral extent of SDR types is shown with the horizontal bars. See Figure 1 for line
420 locations and Figure 2 for a fuller description of SDR type characteristics.

421 **Figure 4.** Gather conditioning in the migrated depth domain. The location of the panels is
422 given in Figure 7. The red line shows the picked Top SDR horizon and all panels have the
423 same amplitude scaling applied. Panels (a) – (c) show the effect of varying the P-cut value
424 during Tau-P multiple suppression. A wide P-cut value (e.g. 250 ms) leaves multiples in the
425 record which are much more effectively removed using a P-cut of 150 ms. Panels (d) – (e)
426 show migrated gathers before and after the angle and outer trace mute application.

427 **Figure 5.** Comparison of a single common-reflection point (CRP) gather depth-migrated
428 during three sequential tomographic updates to the velocity model. The red and pink lines
429 show the picked Top and Base SDR horizon respectively and all panels have the same
430 amplitude scaling applied. Note how the final tomographic update (d) produced the flattest,
431 most continuous reflections, particularly below a depth of 10 km.

432 **Figure 6.** Tomographic inversion results for Line A. In all sections the white dashed line is the
433 computed coherence threshold (i.e. velocity field deeper than this boundary is not
434 constrained). The red and pink lines mark Top and Base SDR as picked from the
435 interpretation of the reflection image alone (Figure 3). (a) Seismic reflection profile
436 underlain by inverted interval velocity field. The depth and lateral resolution of the velocity
437 grid is 200 m and 500 m respectively. (b) Interval velocity field with 0.5 km/s contours. (c)
438 Coherency showing the level of confidence in tomography above the 0.3 threshold. Boxes
439 mark locations of other figures as indicated.

440 **Figure 7.** Tomographic inversion results for Line B. Details as Figure 6.

441 **Figure 8.** Enlarged section of Line A. (a) Seismic reflection profile. (b) Seismic reflection
442 profile underlain by inverted interval velocity field, the coherency threshold indicating the
443 level of confidence in tomography. (c) Interpretation cartoon. (d) Individual velocity-depth
444 profiles subdivided into Type I (red) and Type IIa (blue) SDRs as shown in the interpretation
445 cartoon. For comparison, the black line is a velocity-depth profile extracted from wide-angle
446 seismic profile BGR04-REFR01 (Becker et al., 2014) at the location of profile ii. (e) Stacked
447 velocity-depth profiles across the Type IIa SDRs for the region shown.

448 **Figure 9.** Enlarged section of Line B. Details as Figure 8. Note that the location of profile iii
449 (dashed line) is landward of the seismic section shown in (a-c) but can be seen in Fig.7.

450 **Figure 10.** South American SDR interval velocity-pressure profiles obtained in our study
451 compared to those from the ICEMELT experiment in Iceland (grey, Darbyshire et al., 1998).
452 The conversion from depth to lithospheric pressure for our profiles used a single 3-layer
453 model with densities of water, sediment and SDR-sequence of 1000, 2200 and 2800 kg/m³
454 respectively (Brocher, 2005). The conversion from depth to lithospheric pressure for the
455 Icelandic profiles used a single 2800 kg/m³ layer, and applied a correction for an estimated 3
456 km of material removed by glacial erosion (84 MPa, Siler and Karson, 2017).

457 **9 Acknowledgements**

458 We thank Anton Pavlov and Lauren Braidwood for their assistance in the initial set up of the
459 in-house processing conducted at ION. Part of the analysis also used SeisSpace/ProMax and
460 Kingdom Suite interpretation software provided via grants to Imperial College London from
461 Halliburton and IHS Energy respectively. CM was supported by a Janet Watson PhD
462 studentship from Imperial College London. We thank Fiona Darbyshire for providing a digital
463 copy of the ICEMELT seismic velocity model and Ian Davison for directing us to relevant
464 papers about commercial work in the Pelotas Basin.

465 **10 References**

466

467

468 Abdelmalak, M. M., T. B. Andersen, S. Planke, J. I. Faleide, F. Corfu, C. Tegner, G. E. Shephard, D.
469 Zastrozhnov & R. Myklebust, 2015. The ocean-continent transition in the mid-Norwegian

470 margin: Insight from seismic data and an onshore Caledonian field analogue. *Geology* **43**,
471 1011-1014. DOI: 10.1130/G37086.1

472 Becker, K., D. Franke, R. Trumbull, M. Schnabel, I. Heyde, B. Schreckenberger, H. Koopmann, K.
473 Bauer, W. Jokat & C. M. Krawczyk, 2014. Asymmetry of high-velocity lower crust on the South
474 Atlantic rifted margins and implications for the interplay of magmatism and tectonics in
475 continental breakup. *Solid Earth* **5**, 1011-1026. DOI: 10.5194/se-5-1011-2014

476 Berndt, C., O. P. Skogly, S. Planke, O. Eldholm & R. Mjelde, 2000. High-velocity breakup-related sills
477 in the Voring Basin, off Norway. *Journal of Geophysical Research-Solid Earth* **105**, 28443-
478 28454. Doi 10.1029/2000jb900217

479 Brocher, T. A., 2005. Empirical relations between elastic wavespeeds and density in the earth's crust.
480 *Bulletin of the Seismological Society of America* **95**, 2081-2092. DOI: 10.1785/0120050077

481 Brooks, C. K. & T. F. D. Nielsen, 1982. The E Greenland continental margin: a transition between
482 oceanic and continental magmatism. *Journal of the Geological Society* **139**, 265-275. DOI:
483 10.1144/gsjgs.139.3.0265

484 Buck, W. R., 2017. The role of magmatic loads and rift jumps in generating seaward dipping
485 reflectors on volcanic rifted margins. *Earth and Planetary Science Letters* **466**, 62-69. DOI:
486 10.1016/j.epsl.2017.02.041

487 Christensen, N. I., 1996. Poisson's ratio and crustal seismology. *Journal of Geophysical Research-Solid*
488 *Earth* **101**, 3139-3156. DOI: 10.1029/95jb03446

489 Collier, J. S., C. McDermott, G. Warner, N. Gyori, M. Schnabel, K. McDermott & B. W. Horn, 2017.
490 New constraints on the age and style of continental breakup in the South Atlantic from
491 magnetic anomaly data. *Earth and Planetary Science Letters* **477**, 27-40. DOI:
492 10.1016/j.epsl.2017.08.007

493 Conti, B., J. A. D. Perinotto, G. Veroslaysky, M. G. Castillo, H. D. S. Ana, M. Soto & E. Morales, 2017.
494 Speculative petroleum systems of the southern Pelotas Basin, offshore Uruguay. *Marine and*
495 *Petroleum Geology* **83**, 1-25. 10.1016/j.marpetgeo.2017.02.022

496 Corti, G., A. Agostini, D. Keir, J. Van Wijk, I. D. Bastow & G. Ranalli, 2015. Magma-induced axial
497 subsidence during final-stage rifting: Implications for the development of seaward-dipping
498 reflectors. *Geosphere* **11**, 563-571. DOI: 10.1130/GES01076.1

499 Darbyshire, F. A., I. T. Bjarnason, R. S. White & O. G. Flovenz, 1998. Crustal structure above the
500 Iceland mantle plume imaged by the ICEMELT refraction profile. *Geophysical Journal*
501 *International* **135**, 1131-1149. DOI: 10.1046/j.1365-246X.1998.00701.x

502 Detrick, R., J. Collins, R. Stephen & S. Swift, 1994. In-situ evidence for the nature of the seismic layer
503 2/3 boundary in oceanic-crust. *Nature* **370**, 288-290. DOI: 10.1038/370288a0

504 Eldholm, O., J. Thiede, E. Taylor & S. S. Party, 1987. Summary and preliminary conclusions, ODP Leg
505 104. *In Proceedings of the Ocean Drilling Program, Initial Results. Ed. O. Eldholm, J. Thiede, E.*
506 *Taylor et al., (Ocean Drilling Program). 104 pp. 751-771.*

507 Fliedner, M. M. & R. S. White, 2001. Seismic structure of basalt flows from surface seismic data,
508 borehole measurements, and synthetic seismogram modeling. *Geophysics* **66**, 1925-1936. DOI:
509 10.1190/1.1486760

510 Franke, D., 2013. Rifting, lithosphere breakup and volcanism: Comparison of magma-poor and
511 volcanic rifted margins. *Marine and Petroleum Geology* **43**, 63-87. DOI:
512 10.1016/j.marpetgeo.2012.11.003

513 Franke, D., S. Ladage, M. Schnabel, B. Schreckenberger, C. Reichert, K. Hinz, M. Paterlini, J. de
514 Abelleira & M. Siciliano, 2010. Birth of a volcanic margin off Argentina, South Atlantic.
515 *Geochemistry Geophysics Geosystems* **11**. DOI: 10.1029/2009gc002715

516 Fruehn, J., S. Greenwood, V. Valler & D. Sekulic, 2014. Resolving small-scale near-seabed velocity
517 anomalies using non-parametric autopicking and hybrid tomography. *CSEG Recorder* 1-10.

518 Fruehn, J., I. F. Jones, V. Valler, P. Sangvai, A. Biswal & M. Mathur, 2008. Resolving near-seabed
519 velocity anomalies: Deep water offshore eastern India. *Geophysics* **73**, VE235-VE241. DOI:
520 10.1190/1.2957947

521 Geoffroy, L., 2005. Volcanic passive margins. *Comptes Rendus Geoscience* **337**, 1395-1408. DOI:
522 10.1016/j.crte.2005.10.006

523 Geoffroy, L., J. P. Callot, S. Scaillet, A. Skuce, J. P. Gelard, M. Ravilly, J. Angelier, B. Bonin, C. Cayet, K.
524 Perrot & C. Lepvrier, 2001. Southeast Baffin volcanic margin and the North American-
525 Greenland plate separation. *Tectonics* **20**, 566-584. DOI: 10.1029/2001tc900003

526 Gibson, I. L. & D. Love, 1989. A listric fault model for the formation of the dipping reflectors
527 penetrated during the drilling of hole 642E, ODP leg 104. *In* Proceedings of the Ocean Drilling
528 Program, Scientific Results. *Ed.* O. Eldholm, J. Thiede, E. Taylor et al. 104 pp. 979-983.

529 Goncharov, A. & G. Nelson, 2012. From two way time to depth and pressure for interpretation of
530 seismic velocities offshore: Methodology and examples from the Wallaby Plateau on the West
531 Australian margin. *Tectonophysics* **572**, 26-37. DOI: 10.1016/j.tecto.2012.06.037

532 Gordon, A. C. & W. U. Mohriak, 2015. Seismic volcano-stratigraphy in the basaltic complexes on the
533 rifted margin of Pelotas Basin, southeast Brazil. Petroleum Systems in "Rift" Basins: GCSSEPM
534 34th Annual Conference, Houston, Texas USA pp. 748-786.

535 Hamilton, E. L., 1979. Sound-velocity gradients in marine-sediments. *Journal of the Acoustical Society*
536 *of America* **65**, 909-922. Doi 10.1121/1.382594

537 Hinz, K., 1981. A hypothesis on terrestrial catastrophes: wedges of very thick oceanward dipping
538 layers beneath passive continental margins—their origin and paleoenvironmental significance.
539 *Geologisches Jahrbuch, Reihe E, Geophysik* **22**, 3-28.

540 Jones, I. F., 2010. An introduction to velocity model building, European Association of Geoscientists
541 & Engineers pp. 296.

542 Klausen, M. B. & H. C. Larsen, 2002. East Greenland coast-parallel dike swarm and its role in
543 continental breakup. *In* Volcanic Rifted Margins. *Ed.* M. A. Menzies, S. L. Klemperer, C. J.
544 Ebinger and J. Baker, Geological Society of America Special Publication. 362 pp. 133–158.

545 Larsen, H. C., A. D. Saunders & P. D. Clift, 1994. Proceedings of the Ocean Drilling Program, Initial
546 Reports. College Station, TX Ocean Drilling Program, 152 pp.

547 McDermott, C., L. Lonergan, J. S. Collier, P. Bellingham & K. McDermott, 2018. Characterisation of
548 seaward-dipping reflectors along the S. American Atlantic margin and implications for
549 continental breakup. *Tectonics*. DOI: 10.1029/2017TC004923

550 Mjelde, R., T. Raum, Y. Murai & T. Takanami, 2007. Continent-ocean-transitions: Review, and a new
551 tectono-magmatic model of the Voring Plateau, NE Atlantic. *Journal of Geodynamics* **43**, 374-
552 392. 10.1016/j.jog.2006.09.013

553 Morgan, R. L. & A. B. Watts, 2018. Seismic and gravity constraints on flexural models for the origin of
554 seaward dipping reflectors. *Geophysical Journal International* **214**, 2073-2083. DOI:
555 10.1093/gji/ggy243

556 Mutter, J. C., M. Talwani & P. L. Stoffa, 1982. Origin of seaward-dipping reflectors in oceanic-crust off
557 the Norwegian Margin by subaerial sea-floor spreading. *Geology* **10**, 353-357. DOI:
558 10.1130/0091-7613(1982)10<353:Oosrio>2.0.Co;2

559 Myers, J. S., 1980. Structure of the coastal dyke swarm and associated plutonic intrusions of East
560 Greenland. *Earth and Planetary Science Letters* **46**, 407-418. DOI: 10.1016/0012-
561 821x(80)90054-0

562 Ogilvie, J. S., R. Crompton & N. H. Hardy, 2001. Characterization of volcanic units using detailed
563 velocity analysis in the Atlantic Margin, West of Shetlands, United Kingdom. *The Leading Edge*
564 **20**, 34-50.

565 Paton, D. A., J. Pindell, K. McDermott, P. Bellingham & B. Horn, 2017. Evolution of seaward-dipping
566 reflectors at the onset of oceanic crust formation at volcanic passive margins: Insights from
567 the South Atlantic. *Geology* **45**, 439-442. DOI: 10.1130/G38706.1

568 Planke, S., E. Alvestad & O. Eldholm, 1999. Seismic characteristics of basalt extrusive and intrusive
569 rocks. *The Leading Edge* **18**, 342-348.

570 Planke, S. & O. Eldholm, 1994. Seismic response and construction of seaward dipping wedges of
571 flood basalts - Vøring volcanic margin. *Journal of Geophysical Research-Solid Earth* **99**, 9263-
572 9278. DOI: 10.1029/94jb00468

573 Planke, S., P. A. Symonds, E. Alvestad & J. Skogseid, 2000. Seismic volcanostratigraphy of large-
574 volume basaltic extrusive complexes on rifted margins. *Journal of Geophysical Research-Solid*
575 *Earth* **105**, 19335-19351. DOI: 10.1029/1999jb900005

576 Quirk, D. G., A. Shakerley & M. J. Howe, 2014. A mechanism for construction of volcanic rifted
577 margins during continental breakup. *Geology* **42**, 1079-1082. DOI: 10.1130/G35974.1

578 Roberts, D. G., J. Backman, A. C. Morton, J. W. Murray & J. B. Keene, 1984. Evolution of volcanic
579 rifted margins - Synthesis of Leg-81 results on the west margin of Rockall Plateau. *Initial*
580 *Reports of the Deep Sea Drilling Project* **81**, 883-911. DOI: 10.2973/dsdp.proc.81.139.1984

581 Siler, D. L. & J. A. Karson, 2017. Along-axis structure and crustal construction processes of spreading
582 segments in Iceland: Implications for magmatic rifts. *Tectonics* **36**, 2068-2084. DOI:
583 10.1002/2017tc004629

584 Soto, M., E. Morales, G. Veroslavsky, H. D. Ana, N. Ucha & P. Rodriguez, 2011. The continental
585 margin of Uruguay: Crustal architecture and segmentation. *Marine and Petroleum Geology* **28**,
586 1676-1689. DOI: 10.1016/j.marpetgeo.2011.07.001

587 Spitzer, R., R. S. White & iSIMM_Team, 2005. Advances in seismic imaging through basalts: A case
588 study from the Faroe-Shetland Basin. *Petroleum Geoscience* **11**, 147-156. DOI: 10.1144/1354-
589 079304-639

590 Stica, J. M., P. V. Zalan & A. L. Ferrari, 2014. The evolution of rifting on the volcanic margin of the
591 Pelotas Basin and the contextualization of the Paraná-Etendeka LIP in the separation of
592 Gondwana in the South Atlantic. *Marine and Petroleum Geology* **50**, 1-21. DOI:
593 10.1016/j.marpetgeo.2013.10.015

594 Taposeea, C. A., J. J. Armitage & J. S. Collier, 2016. Asthenosphere and lithosphere structure controls
595 on early onset oceanic crust production in the southern South Atlantic. *Tectonophysics*. DOI:
596 10.1016/j.tecto.2016.06.026

597 White, R. S., L. K. Smith, A. W. Roberts, et al., 2008. Lower-crustal intrusion on the North Atlantic
598 continental margin. *Nature* **452**, 460-464. DOI: 10.1038/nature06687

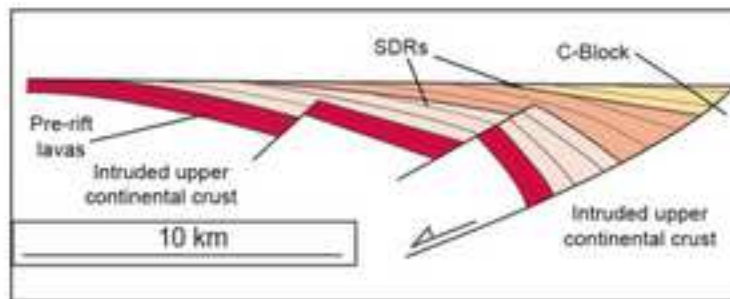
599 Ziolkowski, A., P. Hanssen, R. Gatliff, H. Jakubowicz, A. Dobson, G. Hampson, X.-Y. Li & E. Liu, 2003.

600 Use of low frequencies for sub basalt imaging. *Geophysical Prospecting* **51**, 169-182.

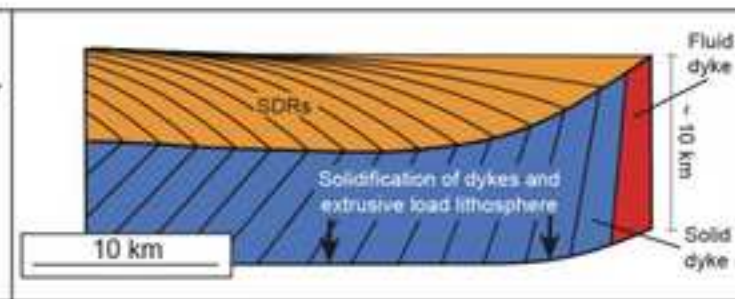
601

602

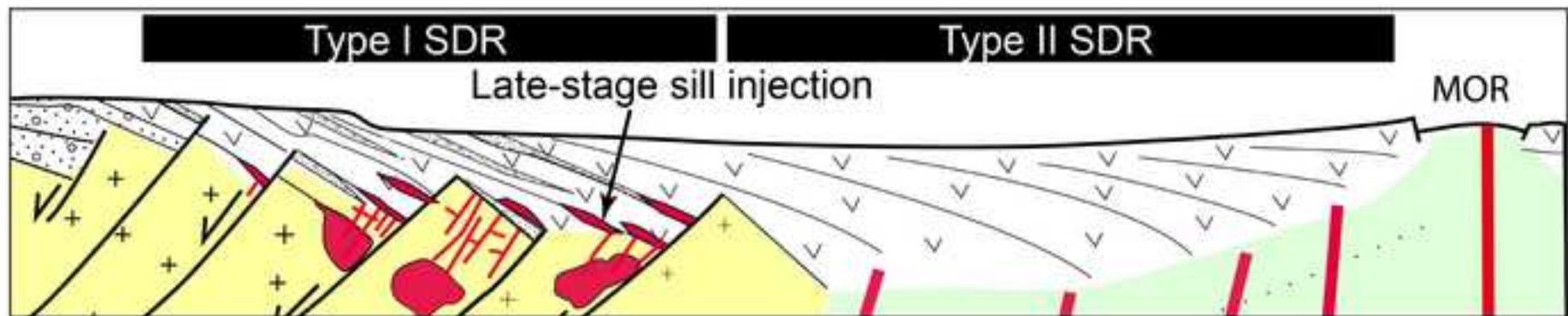
Geoffroy, 2005



Buck, 2017



This study:



Continental crust
SDR dip due to footwall rotation

Magmatic crust
SDR dip due to magmatic loading

Figure

[Click here to download Figure: Figs_revision_small_all.pdf](#)

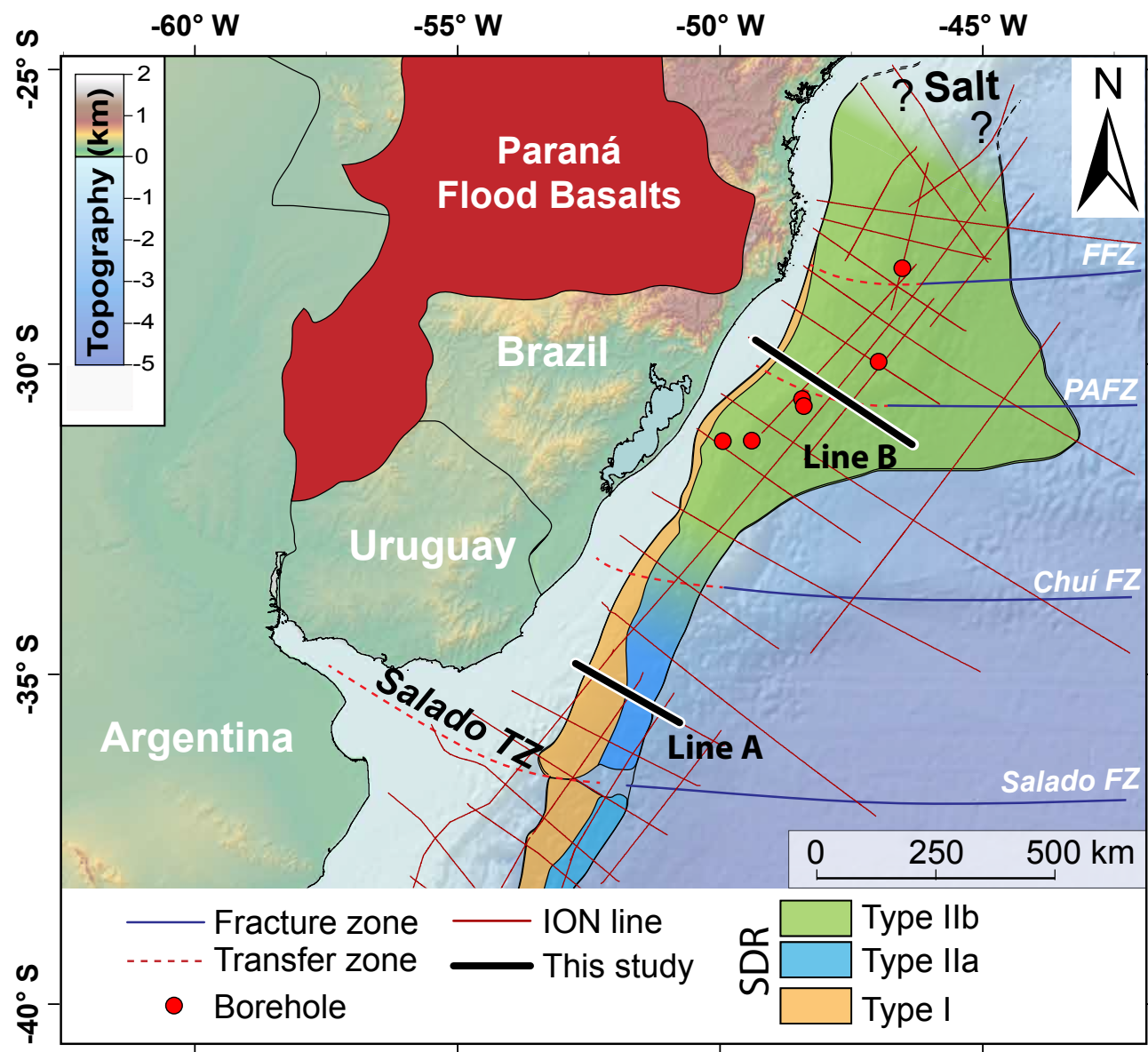


Figure 1

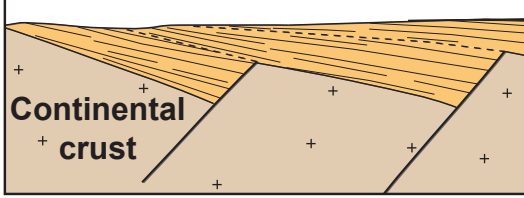
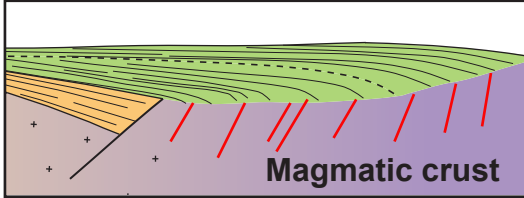
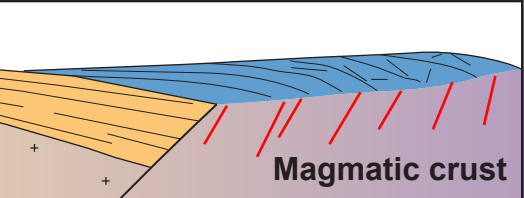
Type I	Sub-aerial	<p style="text-align: center;">~ 40 km</p>  <p>Continental crust</p>
Type IIb	Sub-aerial	<p style="text-align: center;">> 100 km</p>  <p>Magmatic crust</p>
Type IIa	Sub-aerial, elevated	<p style="text-align: center;">~50 km</p>  <p>Magmatic crust</p>

Figure 2

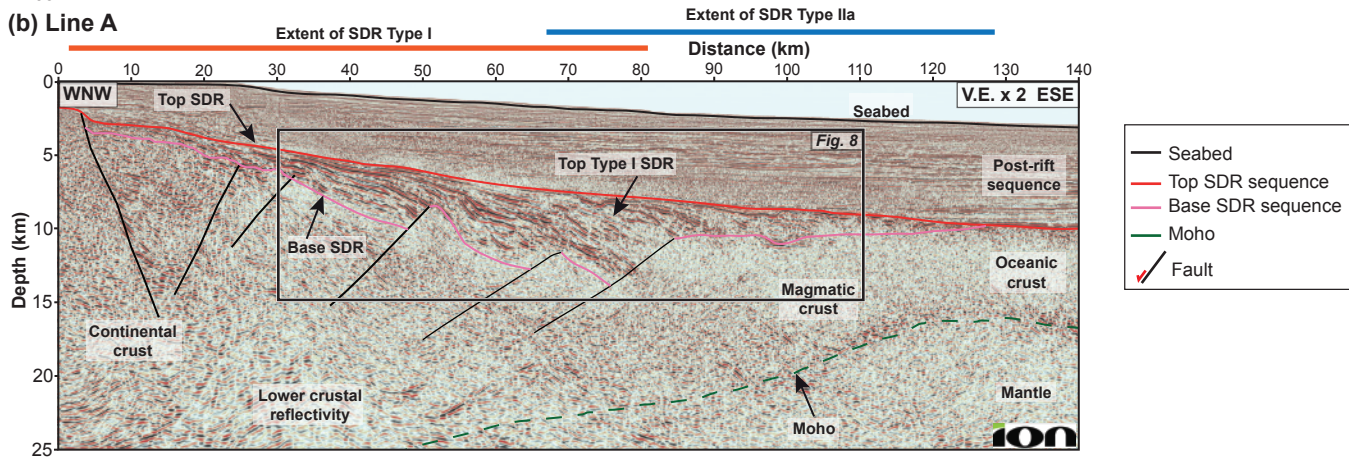
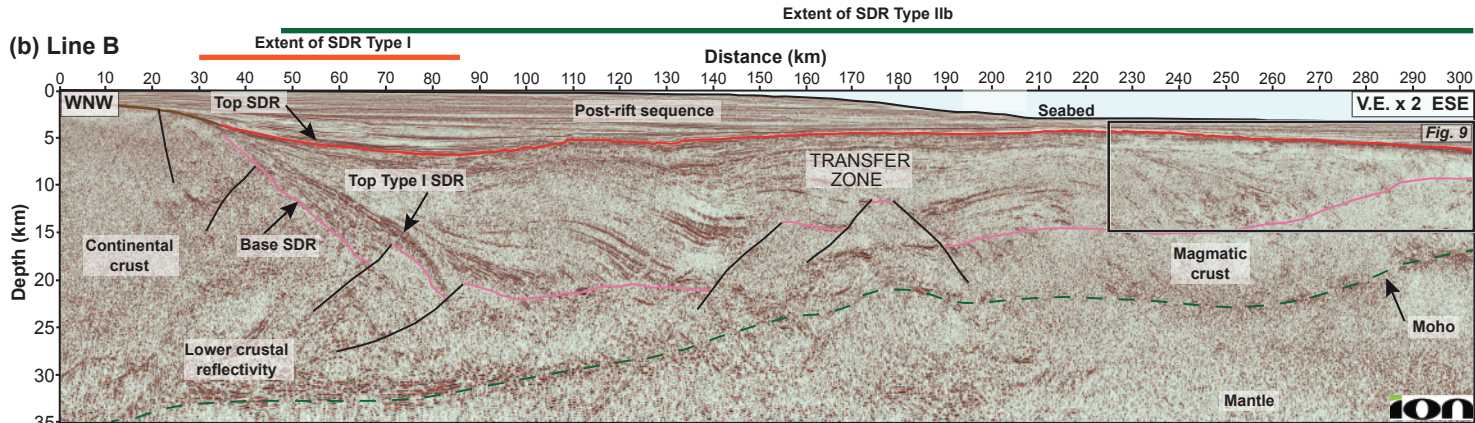


Figure 3

Line B

0.019

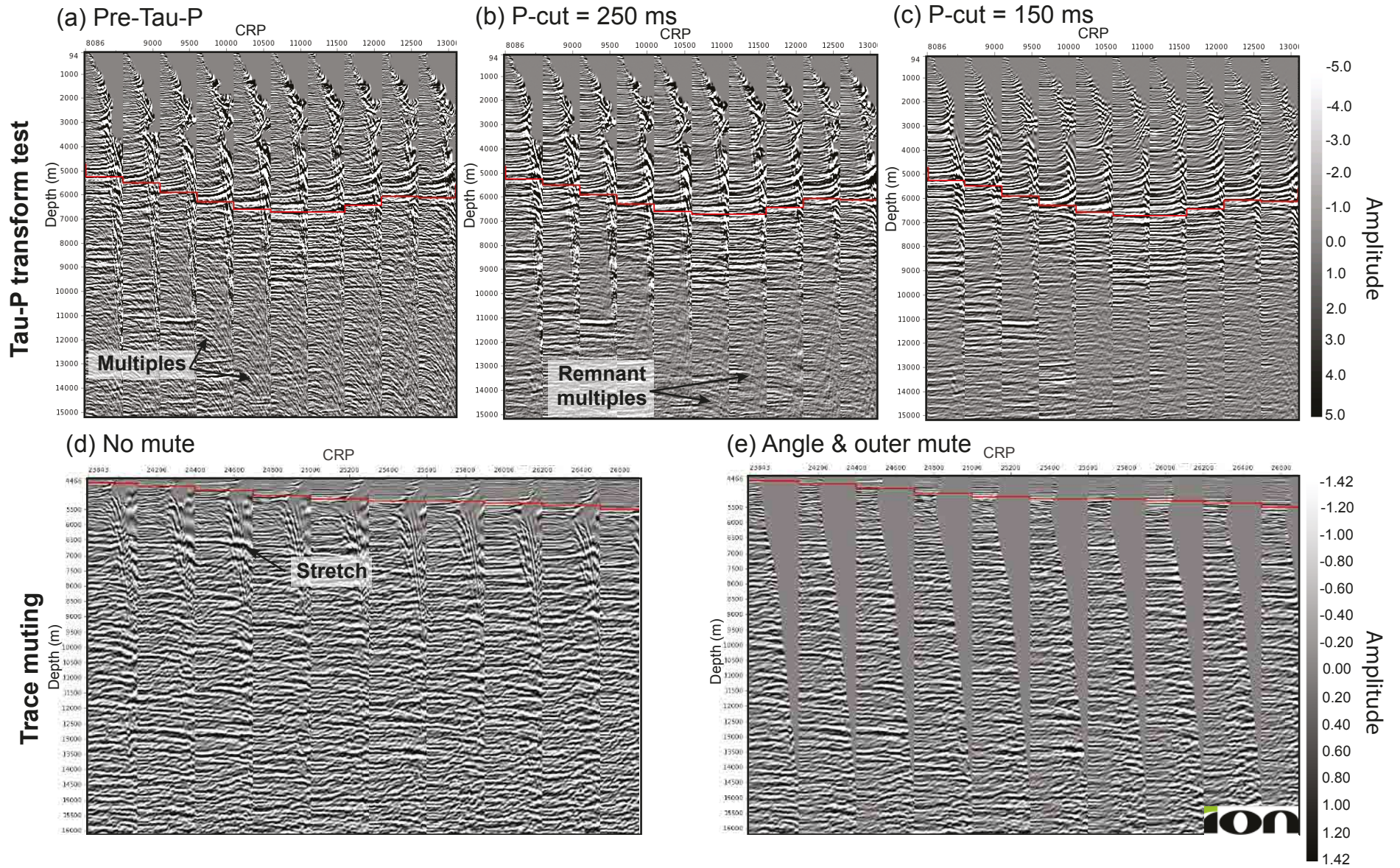


Figure 4

Line B

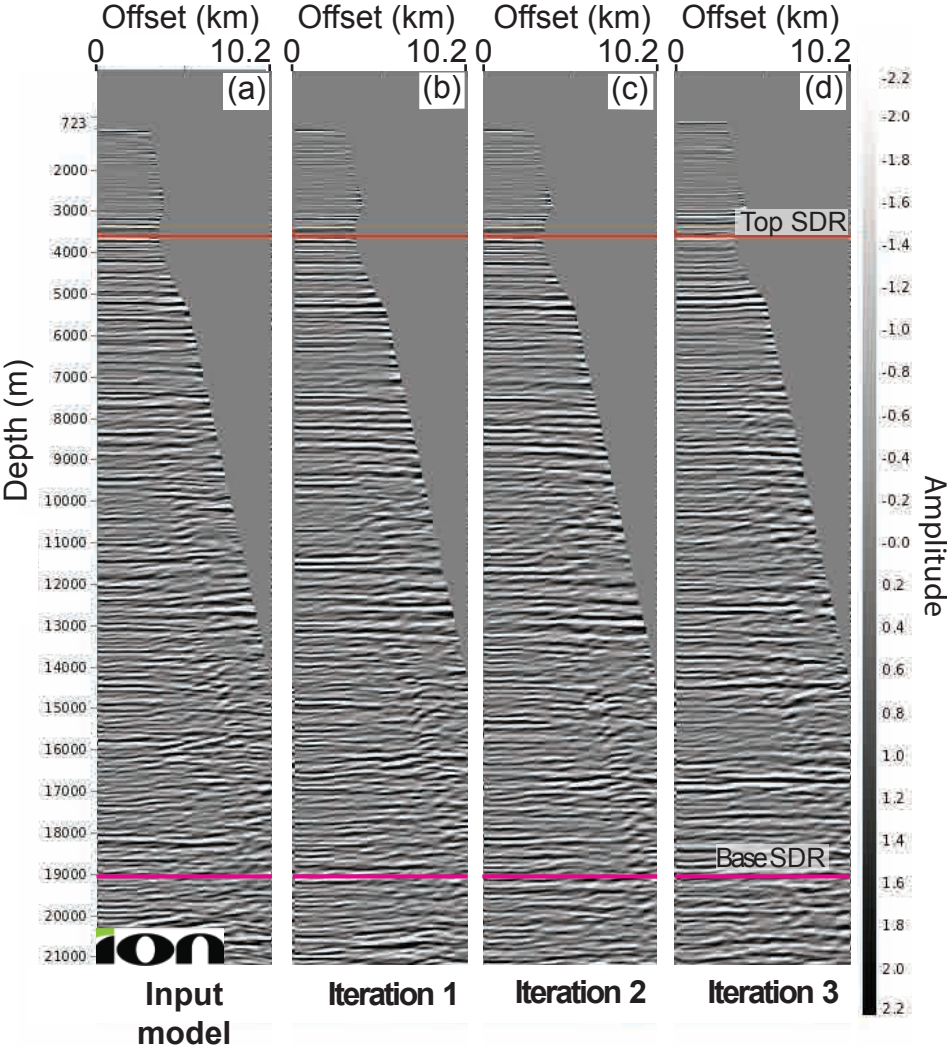


Figure 5

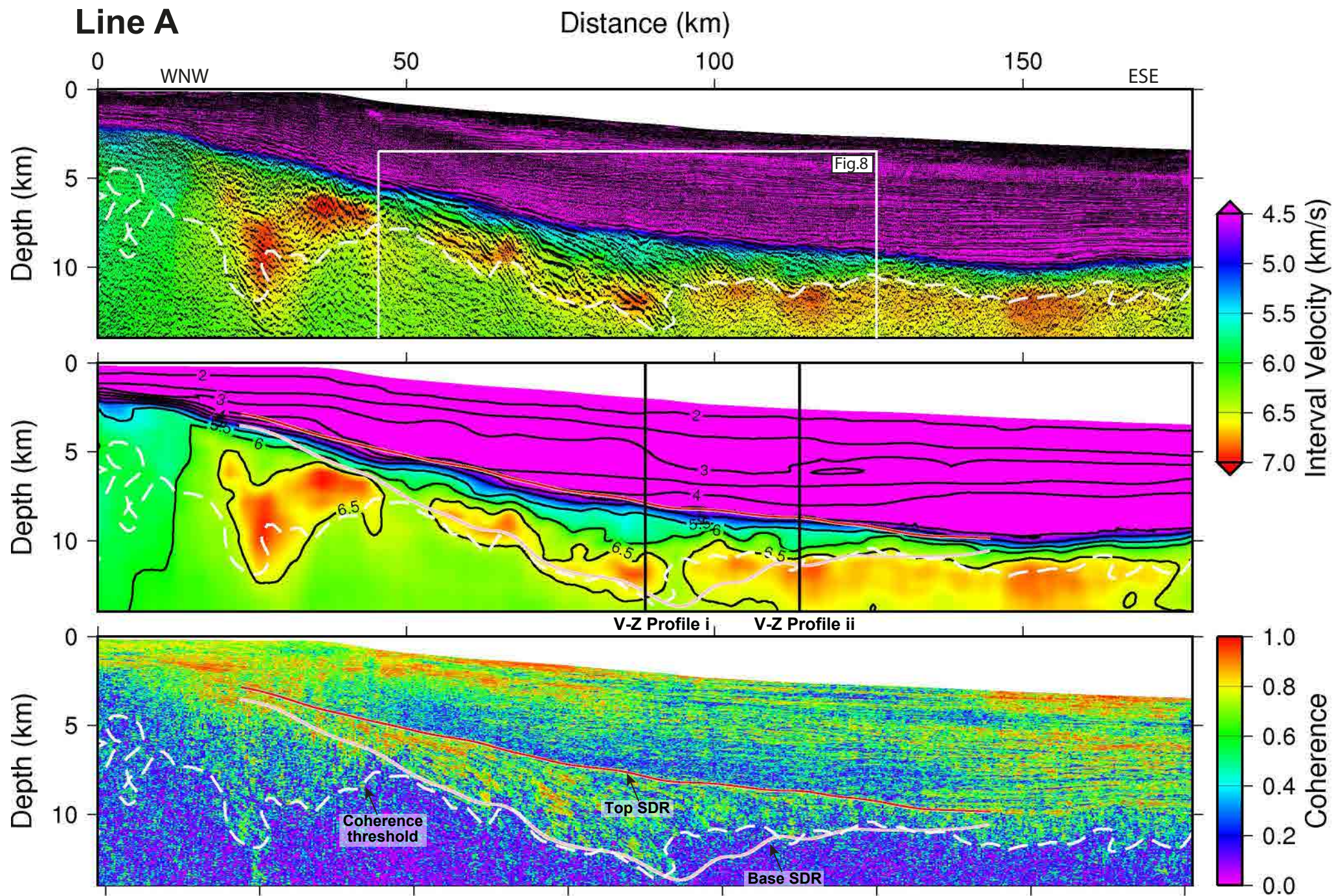


Figure 6

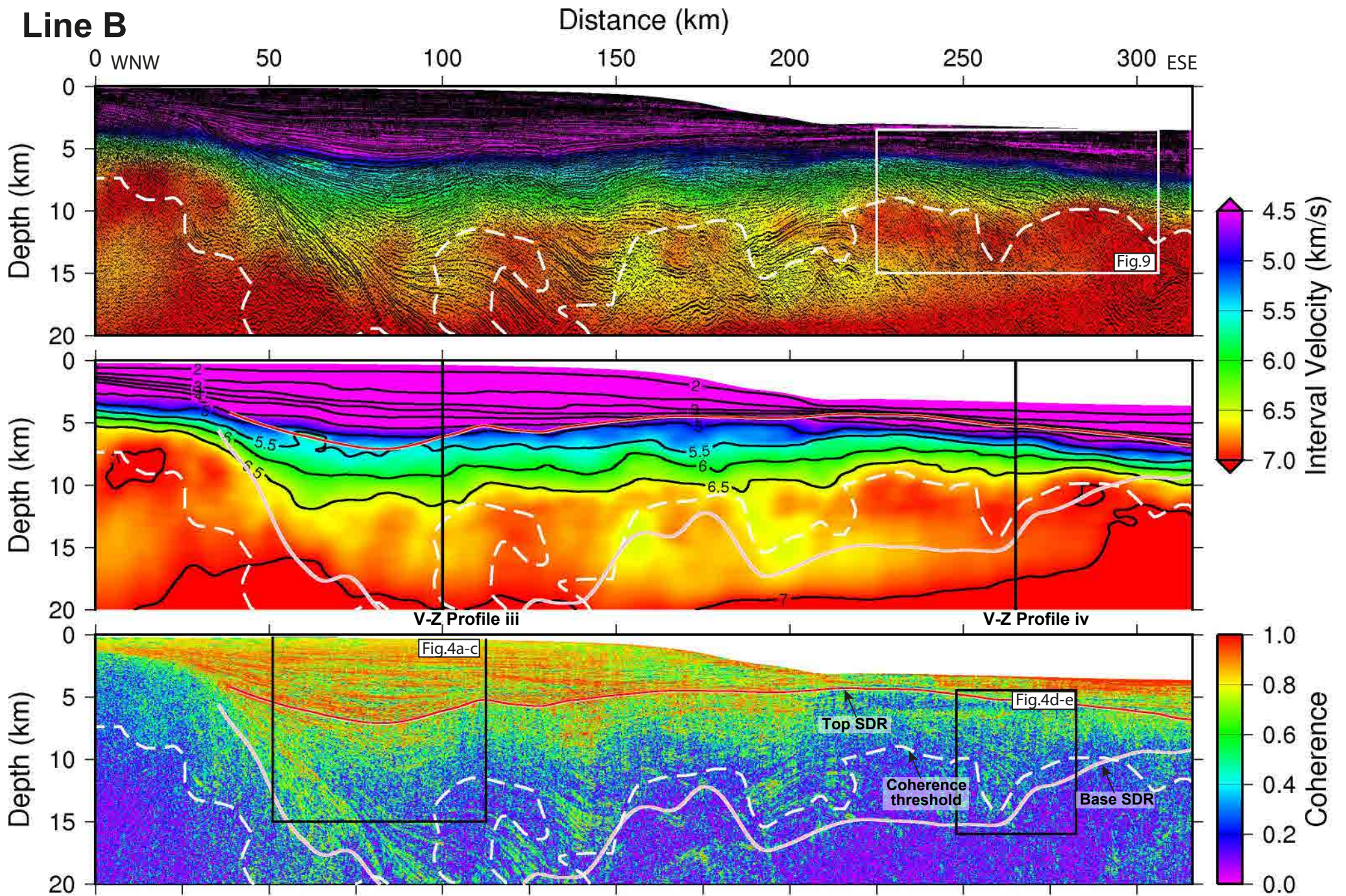


Figure 7

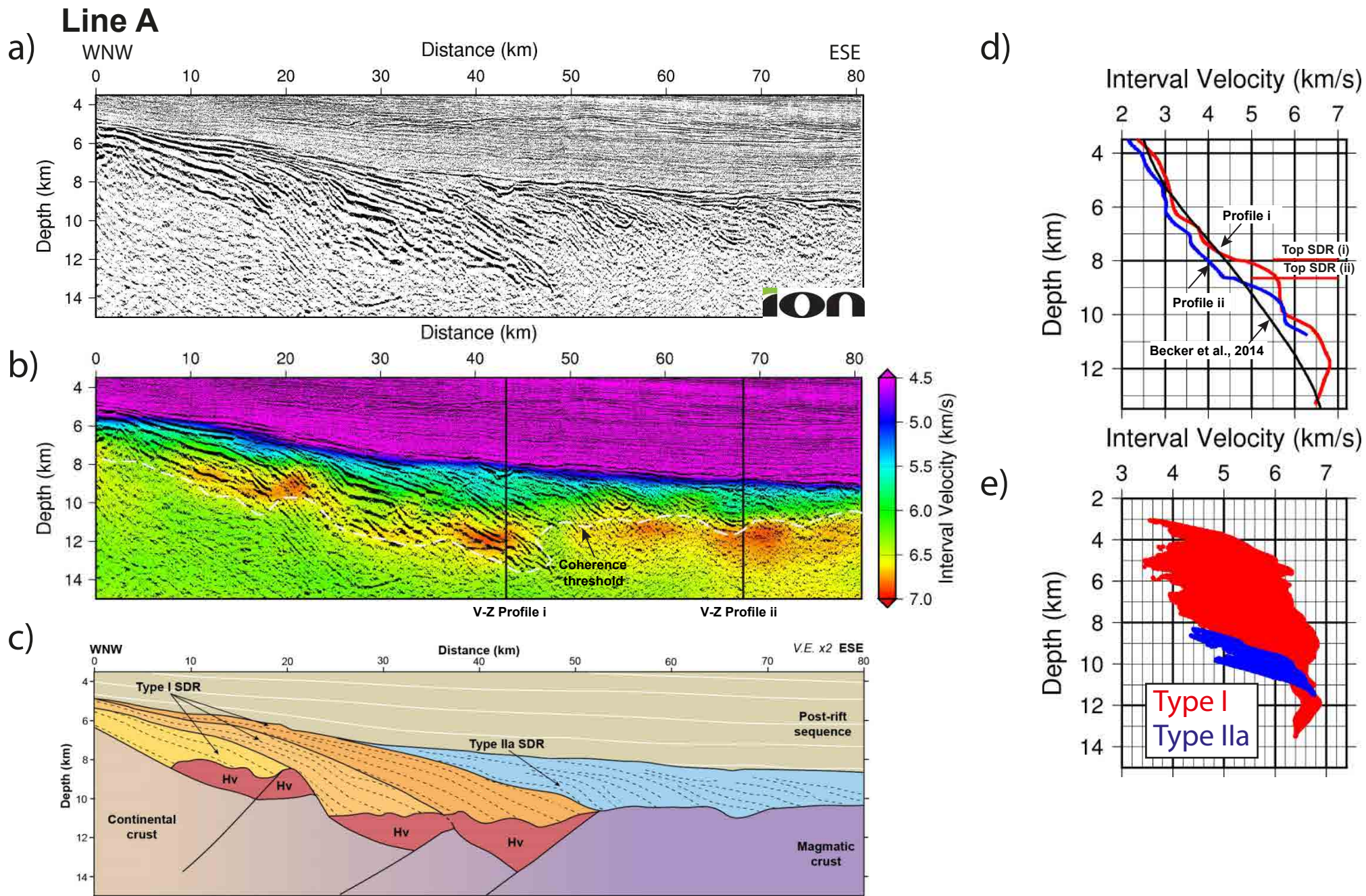


Figure 8

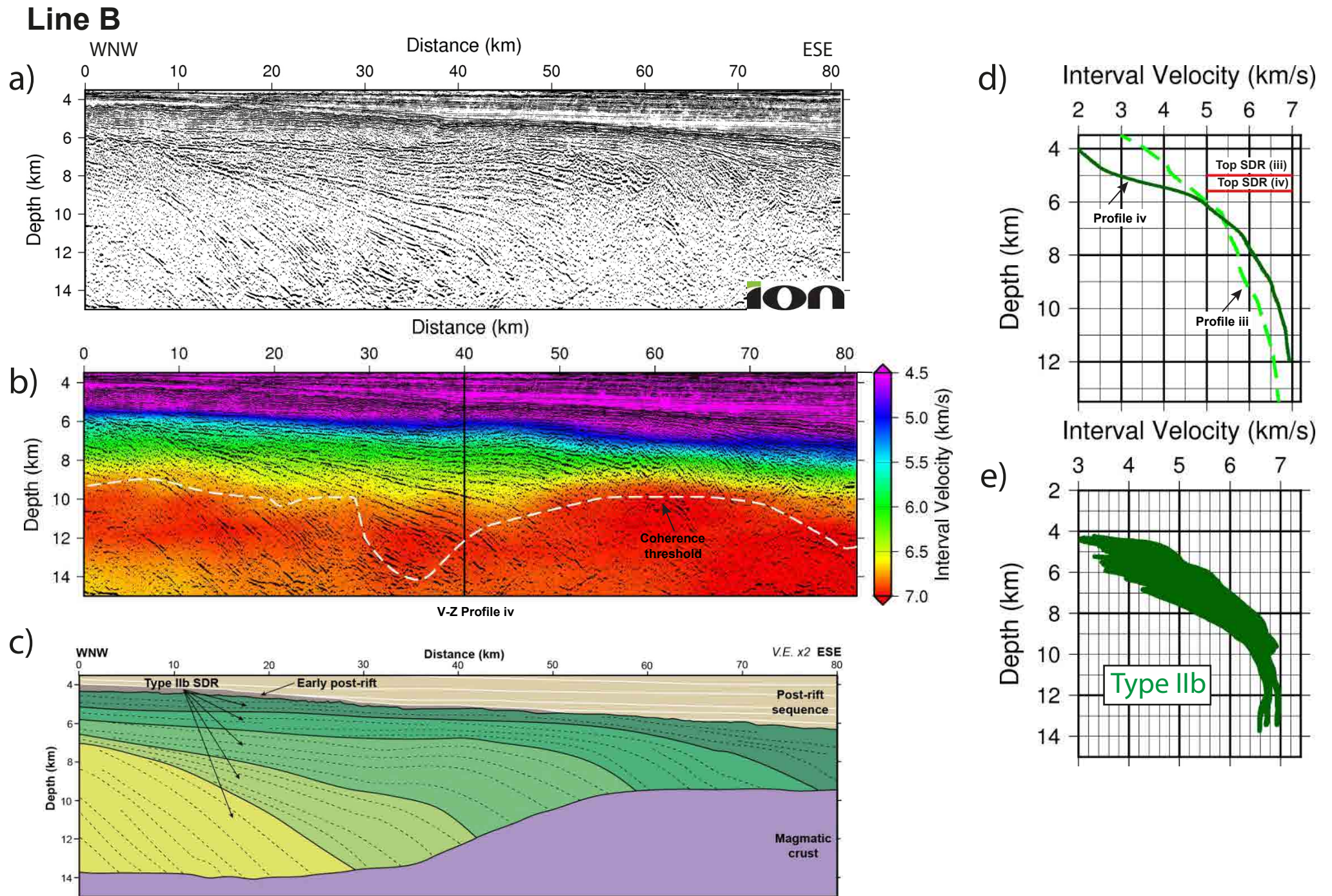


Figure 9

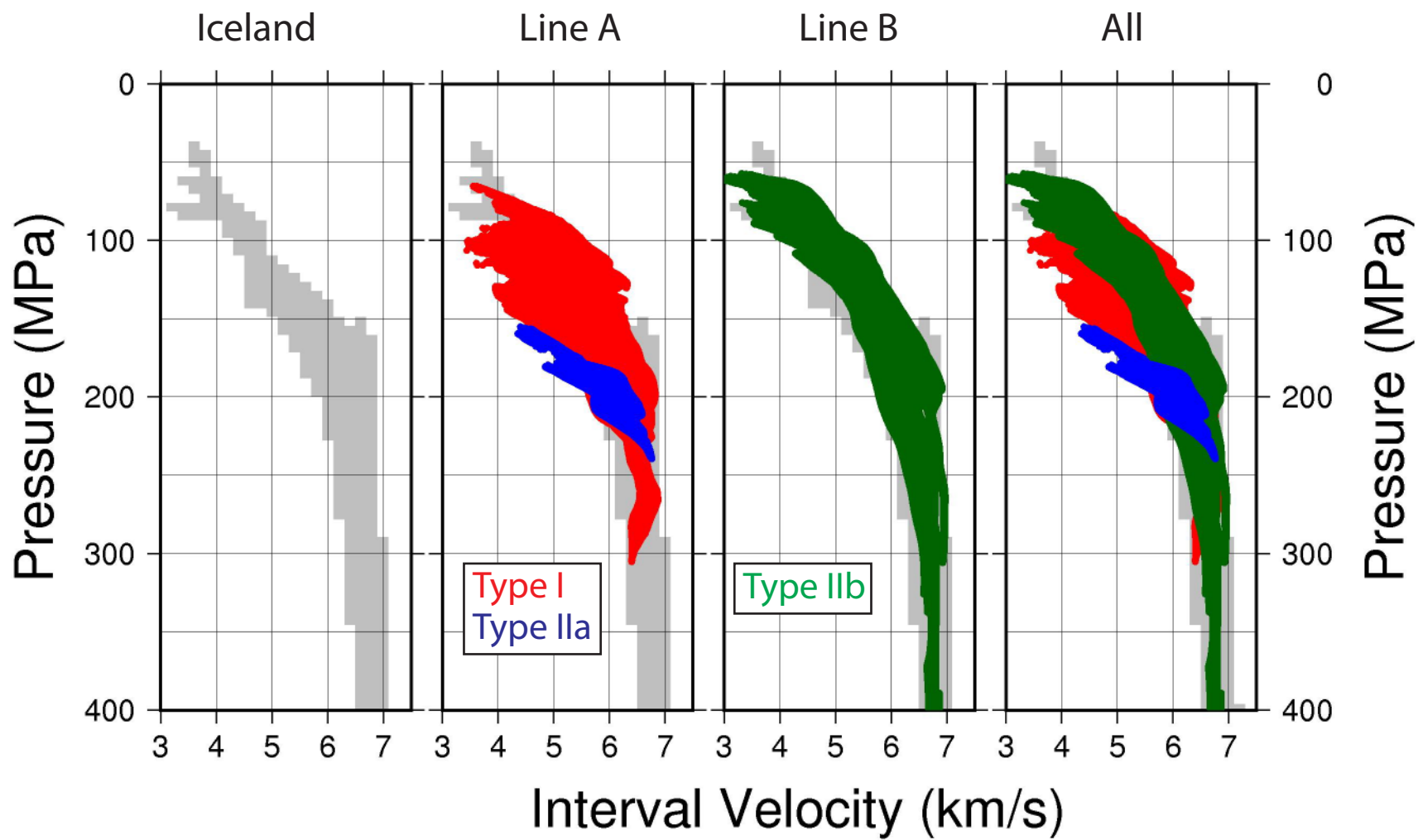


Figure 10